

Energy-Based Scatter Corrections for Scintillation Camera Images of Iodine-131

Kenneth R. Pollard, Thomas K. Lewellen, Mitchell S. Kaplan, David R. Haynor, Robert S. Miyaoka, Janet F. Eary and Lawrence D. Durack

University of Washington Medical Center, Seattle, Washington

The use of high-dose ^{131}I antibody therapy requires accurate measurement of normal tissue uptake to optimize the therapeutic dose. One of the factors limiting the accuracy of such measurements is scatter and collimator septal penetration. This study evaluated two classes of energy-based scatter corrections for quantitative ^{131}I imaging: window-based and spectrum-fitting. **Methods:** The window-based approaches estimate scatter from data in two or three energy windows placed on either side of the 364-keV photopeak using empirical weighting factors. A set of images from spheres in an elliptical phantom were used to evaluate each of the window-based corrections. The spectrum-fitting technique estimates detected scatter at each pixel by fitting the observed energy spectrum with a function that models the photopeak and scatter, and which incorporates the response function of the camera. This technique was evaluated using a set of Rollo phantom images. **Results:** All of the window-based methods performed significantly better than a single photopeak window (338–389 keV), but the weighting factors were found to depend on the object being imaged. For images contaminated with scatter, the spectrum-fitting method significantly improved quantitation over photopeak windowing. Little difference, however, between any of the methods was observed for images containing small amounts of scatter. **Conclusion:** Most clinical ^{131}I imaging protocols will benefit from qualitative and quantitative improvements provided by the spectrum-fitting scatter correction. The technique offers the practical advantage that it does not require phantom-based calibrations. Finally, our results suggest that septal penetration and scatter in the collimator and other detector-head components are important sources of error in quantitative ^{131}I images.

Key Words: scatter correction; iodine-131-imaging; scintillation cameras; window-based technique; spectrum-fitting technique

J Nucl Med 1996; 37:2030–2037

Iodine-131-labeled monoclonal antibodies are used to treat various cancers. At our institution, the patient is first imaged with low-dose ^{131}I -labeled antibodies to determine both tumor and normal tissue uptake (1). The therapeutic dose can then be optimized to deliver the maximum dose to the tumor that will not result in exceeding the normal tissue dose limits. A limitation to this optimization process (and thus a limit to the maximum useable dose) is the accuracy of the measured ^{131}I distribution. Scatter corrected diagnostic images that contain less than 5% bias in the relevant region-of-interest (ROI) is preferable.

Iodine-131 is more difficult to image than $^{99\text{m}}\text{Tc}$ because $^{99\text{m}}\text{Tc}$ is a monoenergetic (140 keV) gamma-ray source, while ^{131}I has multiple gamma-ray emissions [284 keV (5.8%), 364 keV (82%), 637 keV (6.5%) and 723 keV (1.7%)]. Most scintillation cameras are optimized for imaging at 140 keV. Penetration of the septa in high-energy collimators, as well as

scatter in the collimator and detector assembly, can significantly affect the quality of data acquired at and above 364 keV. Also, although the two higher energy emissions are usually ignored, they often scatter in the patient and produce significant bias in ^{131}I images (2–4). Still, a number of techniques developed to correct for object (patient) scatter in $^{99\text{m}}\text{Tc}$ images have been applied to ^{131}I imaging (4–10).

Collimator

Many high energy collimators are optimized for 364 keV and allow substantial penetration of the higher energy photons emitted by ^{131}I . The combination of septal penetration and the relatively low attenuation of the higher energy gamma rays by the patient's body means these photons often contribute a significant fraction of the events collected by the imaging system.

Septal-penetration for a parallel-hole collimator can be estimated as (11):

$$\% \text{ penetration} = 100 \cdot e^{-\mu w}, \quad \text{Eq. 1}$$

where μ is the linear attenuation coefficient of the collimator material (usually lead) at a given energy, and w is the minimum distance through a septum. Hal Anger (1964) stated that "acceptable images result when the narrow beam attenuation of gamma rays taking the [shortest septal] path ... is 95% or more." Although this 5% requirement is considered standard for collimator designs, Kibby (12) and Ostertag et al. (13) suggest that septal penetration should be kept below 1–2%.

A typical high-energy, general-purpose, parallel-hole collimator used for imaging ^{131}I has a minimum path of approximately 9.6 mm (w). From Equation 1, septal penetration is 4.8% at 364 keV, 29% at 637 keV and 34% at 723 keV. Even neglecting gamma rays that scatter in the collimator, there is considerable flux of higher-energy photons after the collimator.

Equation 1 assumes that all interactions in a collimator are photoelectric, ignoring the effect of scatter in the collimator. This is a good approximation for lead at 140 keV, based on practical imaging experience and results from Monte Carlo simulations. At 364 keV, however, the absorption probability (probability of photoelectric absorption, given an interaction) in lead is 67%; at 723 keV it is only 40%. This means a 723 keV gamma ray is more likely to Compton scatter in lead than be absorbed. Equation 1 overestimates the collimation effect at 723 keV because it does not account for scattering. Previous work in our laboratory indicated that in a typical study at least 20% of the counts in a 338–389 keV photopeak window result from higher-energy emissions (14).

Based on measured and simulated data, we developed a model of the detected energy spectrum in air (15). The measured spectrum from a 662 keV (^{137}Cs) source in air is nearly constant in the 338–389 keV region. We infer that the high-energy gamma rays (637 keV and 723 keV) that scatter in the crystal produce a relatively flat spectrum in the 364 keV

Received May 22, 1995; revision accepted Jan. 3, 1996.

For correspondence or reprints contact: Tom K. Lewellen, Professor, Radiology Imaging Research Laboratory, University of Washington Medical Center Box 356004, Seattle, WA 98195-6004.

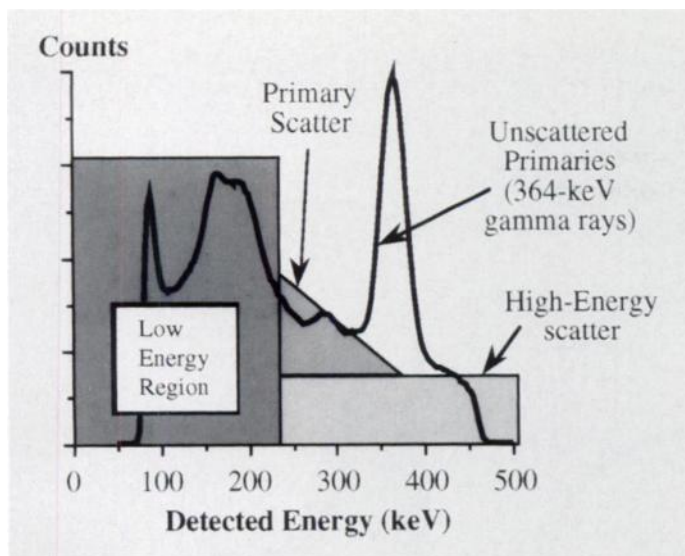


FIGURE 1. Conceptual model of the detected ^{131}I spectrum. The pedestal represents scatter contributions from the 637 and 723 keV gamma rays. Primary (364 keV) contributions in the 364-keV regions include scattered and unscattered events. The cutoff for the low energy region is approximate, but events detected with energies in this region are not useful for estimating the scatter distribution in the 364-keV region.

range (Fig. 1). The triangular region just below the 364 keV photopeak is caused by 364 keV photons, these photons scatter in the collimator or detector housing. The lower end of the spectrum results primarily from backscatter and low energy emissions from ^{131}I . It is unlikely that data below 240 keV will provide useful information for estimating scatter in the 364 keV region. The detected energy spectrum for ^{131}I in a scattering medium is qualitatively similar, although detected scatter is increased relative to the size of the photopeak.

Scatter Corrections

Five different window-based scatter corrections were investigated. The technique referred to as lower-window subtraction follows that of Jaszczak et al. (16). The two dual-photopeak methods are similar to those described by King et al. (17). Use of an upper-energy window to estimate and compensate for contributions from the higher-energy emissions of ^{131}I is described by Pentlow (18), Pollard et al. (3) and Macey et al. (9). All reported improved quantitation using upper window data.

The five window-based correction methods are:

Lower-window subtraction:

$$\begin{aligned} (\text{corrected image}) &= (\text{photopeak image}) \\ &- k_{lo} \cdot (\text{lower-window image}). \end{aligned} \quad \text{Eq. 2}$$

Upper-window subtraction:

$$\begin{aligned} (\text{corrected image}) &= (\text{photopeak image}) \\ &- k_{hi} \cdot (\text{upper-window image}). \end{aligned} \quad \text{Eq. 3}$$

Upper- and lower-window subtraction:

$$\begin{aligned} (\text{corrected image}) &= (\text{photopeak image}) \\ &- k_{lo} \cdot (\text{lower-window image}) \\ &- k_{hi} \cdot (\text{upper-window image}). \end{aligned} \quad \text{Eq. 4}$$

Linear dual-photopeak:

$$\begin{aligned} (\text{corrected image}) &= (\text{photopeak image}) \\ &\cdot \left[1 - k_{dpw} \cdot \left(\frac{\text{lower-half image}}{\text{upper-half image}} \right) \right]. \end{aligned} \quad \text{Eq. 5}$$

Nonlinear dual-photopeak:

$$\begin{aligned} (\text{corrected image}) &= (\text{photopeak image}) \\ &\cdot \left[1 - k_{dpw'} \cdot \left(\frac{\text{lower-half image}}{\text{upper-half image}} \right)^{p_{dpw}} \right]. \end{aligned} \quad \text{Eq. 6}$$

where photopeak = 338–389 keV, lower = 268–320 keV, upper = 400–425 keV, lower-half = 338–363 keV, upper-half = 364–389 keV and k_{lo} , k_{hi} , k_{dpw} , $k_{dpw'}$ and p_{dpw} = constants determined with calibration phantoms.

A spectrum-fitting scatter correction algorithm was also investigated. This method models the detected energy spectrum as the sum of a Dirac delta function (the photopeak) and a scatter model spectrum convolved with the energy point-spread function (EPSF). The EPSF represents the measured camera response to a source in air. Initial application of this method to simulated ^{99m}Tc images (19), real ^{99m}Tc images (20), and real ^{131}I images (4) were previously presented.

The observed energy spectrum is given by:

$$g(O) = \int K(O, E) f(E) dE, \quad \text{Eq. 7}$$

where O is the observed energy, E is the true energy, g is the observed energy function, f is the true energy function and K is the transfer function representing the scintillation detector system (21). K is determined at 364 keV from the measured EPSF (assumed to be spatially invariant) and the width was assumed to vary as the square-root of the energy.

The observed energy function in the region near the photopeak is modeled as the sum of a delta function at the photopeak and a scatter model spectrum, convolved with the measured energy response function (21). The incident scatter spectrum is

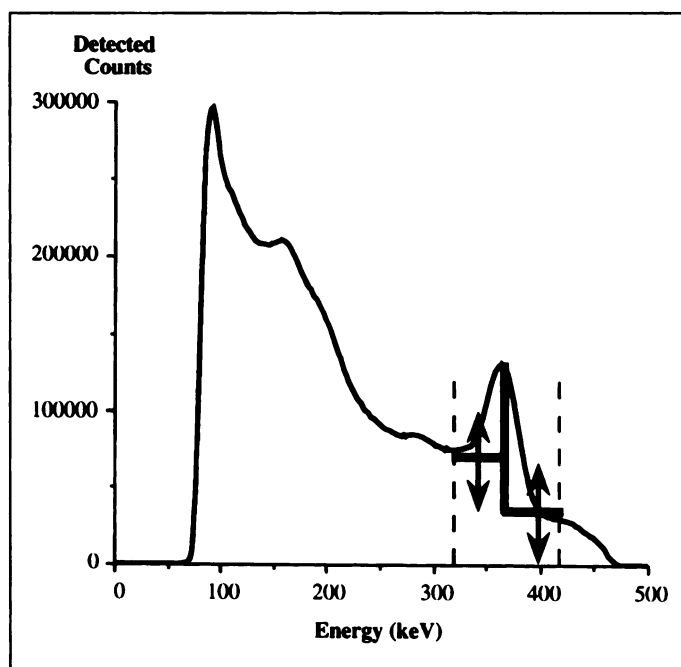


FIGURE 2. Model used in spectrum-fitting routine. The model, a split-pedestal plus a delta function, is shown before convolution with the scatter free spectrum shape derived from a point source.

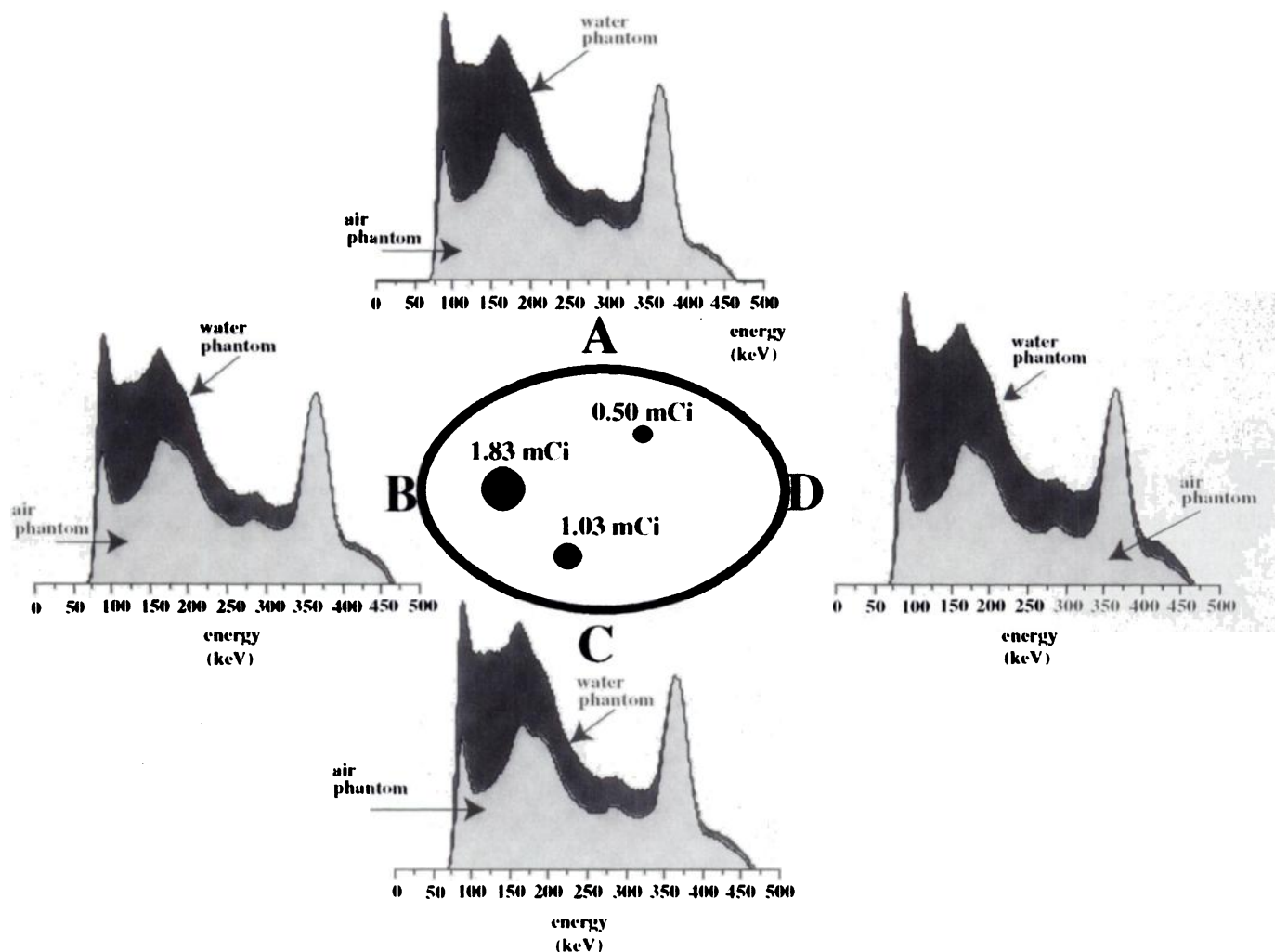


FIGURE 3. Examples of measured energy spectrum for four spherical sources in an elliptical phantom for four different projections. The spectra are shown for the tank filled with water and air. The letters are used to identify the four projections (view angles).

modeled as a split pedestal to account for different (relatively flat) contributions above and below the photopeak (Fig. 2).

Data were binned into 25 sequential 4-keV windows and the spectrum at each pixel was fit over the range of 315–415 keV. The fits were performed using a positivity-constrained least squares method previously described (21). The lower limit was chosen to minimize contamination by the 284 keV emission and the upper limit was chosen to be below the upper-level cutoff of the GE 3000 XC/T used for the experiments. The coefficient of the delta function returned by the fit provided the estimate of unscattered (primary) gamma rays at that pixel in the image.

MATERIALS AND METHODS

Collimator

The effects of septal penetration on the energy response were measured. With the high-energy collimator in place, we acquired images of ^{99m}Tc and ^{131}I line-sources in air at 0, 5, 10, 15 and 20 cm from the collimator face. The high-energy collimator is essentially opaque to the ^{99m}Tc gamma rays, so these images reflect a near-ideal geometric line-spread. The image of the ^{131}I line will be degraded by septal penetration, septal scatter, and backscatter occurring in the detector assembly. The observed differences in the line-spread functions were attributed to these effects.

Multiwindow Corrections

A Data Spectrum elliptical phantom (model 2230, Chapel Hill, NC) was imaged. Three hollow spheres were filled with ^{131}I of uniform concentration. The phantom was imaged from four directions as indicated in Figure 3. The phantom data were used to evaluate the five different window based scatter corrections defined in Equations 2–6.

For these experiments, the “true” activity distribution, N_{true} , was approximated as

$$N_{\text{true}} = N_{\text{air}} e^{-\mu x}, \quad \text{Eq. 8}$$

where N_{air} = number of counts in an ROI obtained from the image taken with no water in the phantom, μ = narrow-beam attenuation coefficient of 364 keV photons in water (0.110 cm^{-1}) and x = distance from sphere center to phantom edge.

We investigated the accuracy of the window-based scatter corrections by optimizing the correction parameters (e.g., k in the Compton subtraction method) for each view-angle, as well as with data from all four view angles combined.

For each individual view, angle the optimization went as follows:

1. Draw 8 ROIs on each image: 3 source ROIs and 5 large background ROIs.
2. Create a corrected ROI, as in Equation 8.

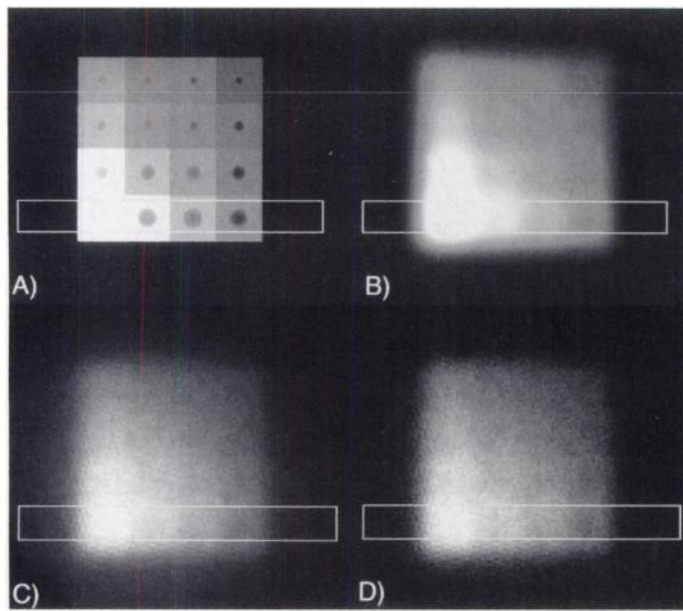


FIGURE 4. Examples of Rollo phantom images. (A) Ideal numerical model image. (B) Ideal image convolved with measured line spread function of collimator at 20 cm. (C) Measured image with high energy collimator and 338–389 keV energy window. (D) Measured image after scatter correction with energy spectrum-fitting algorithm. The rectangular region of interest defines the area used to generate the profiles for Figure 7.

3. For the source ROIs, subtract the true value from the corrected ROI total to determine the error.
4. Add the squares of the error.
5. Minimize the sum-squared-error by altering the parameter(s), such as k , subject to the constraint that the corrected background ROIs remain positive.

For the combined view-angle data, 12 ($=4 \times 3$) source ROIs and 20 ($=4 \times 5$) background ROIs were used for each optimization.

Spectrum-Fitting Scatter Correction

To test the spectrum-fitting method, a Rollo phantom filled with 185 MBq ^{131}I was imaged with a GE 3000 XC/T gamma camera modified to acquire position and energy (xyE) data in list-mode (22,23). The front face of the Rollo phantom was placed 15 cm from the front face of the high-energy parallel-hole collimator, so the center of the Rollo phantom was approximately 20 cm from the front of the collimator. Data were acquired with 0, 5, 10 and 15 cm of Lucite between the collimator and the phantom.

The Rollo phantom (24) consists of a 4×4 array of 2-in. square cells with a solid Lucite sphere centered in each cell (Fig. 4A). The cells vary in thickness and there are four different sphere diameters. Figure 4B depicts a numerical model of the Rollo phantom convolved with the measured resolution of an ^{131}I line source at 20 cm. With the poor spatial resolution of the high-energy collimator, it is not possible to meaningfully measure the contrast between the cold spheres and the hot background. Thus, only the average activity in each square was calculated. To estimate the accuracy of the various images, we used an error measurement based on the correlation coefficient, CC, given by:

$$CC = \frac{\sum (x - \langle x \rangle)(y - \langle y \rangle)}{\sqrt{\sum (x - \langle x \rangle)^2 \sum (y - \langle y \rangle)^2}}, \quad \text{Eq. 9}$$

where x is the number of counts in a pixel of the convolved-ideal image, y is the number of counts in a pixel of the measured (corrected) Rollo image, $\langle x \rangle$ and $\langle y \rangle$ are average pixel values for each image, and the sums are over all pixels in each respective image.

TABLE 1
Comparison of Constants and Associated Errors*

Correction method	Parameter	A only	B only	C only	D only	Combined
Lower window	k_{lo}	0.52	0.67	0.72	0.70	0.64
	Error	1.69	0.49	3.70	0.10	11.5
Upper window	k_{hi}	3.80	3.32	3.44	3.07	3.07
	Error	1.14	16.6	17.4	3.07	53.1
Upper and lower window	k_{lo}	-0.06	0.58	0.48	0.80	0.54
	k_{hi}	3.59	0.64	1.88	-0.44	0.73
	Error	0.90	0.48	3.56	0.05	11.0
Linear dual-photopeak	k_{dpw}	0.20	0.24	0.25	0.33	0.23
	Error	3.68	0.78	5.50	0.29	13.8
Nonlinear dual-photopeak	k_{dpw}	0.25	0.42	0.50	0.45	0.28
	p_{dpw}	2.22	4.16	7.73	2.59	2.24
	Error	3.32	0.47	4.51	0.19	12.6

*error = sum of squares error for the optimization $\times 10^{-6}$.

Obtained for the multi-window scatter correction applied to spheres in an elliptical phantom. The parameter abbreviations are defined in the text (Eq. 2–6). The views used to derive the constants (A, B, C, D) are defined in Figure 3.

The convolved-ideal Rollo image used in the analysis was noise-free. To estimate the error caused by Poisson counting statistics, a set of noisy images was created from the convolved-ideal Rollo data. The level of noise corresponds to the number of counts in the image, for example, 1, 3 or 5 million total counts with a 338 to 389 keV window (covering the range of total image counts seen in typical diagnostic planar ^{131}I -antibody images of patients). These noisy images were then compared to the noise-free convolved Rollo image using the correlation coefficient measure.

RESULTS

Collimator

As expected, the spatial resolution determined from profiles across the line-source images was consistently worse for ^{131}I than for ^{99m}Tc . On the collimator surface, the ratio of the ^{131}I full width at half maximum (FWHM) to the ^{99m}Tc FWHM was 1.2. The ratio increased as the line source was moved farther from the collimator reaching a value of 1.35 at 20 cm. This difference is primarily caused by septal penetration of the ^{131}I gamma rays.

Window-Based Scatter Corrections

Whole-image energy spectra acquired from each of the four sides, with and without water in the phantom are seen in Figure 3. The spectra were normalized to match the heights of the 364-keV photopeaks. This facilitates comparison of the relative amounts of scatter for a deeply buried source (view D) and a source close to the surface (view B). It is instructive to examine the energy spectra associated with the ROIs at different locations in the image. For a ROI centered over a sphere, the high-energy-scatter pedestal is nearly absent. If the ROI is placed midway between two spheres, a high-energy pedestal, a strong Compton region, and a strong photopeak are all seen. For a ROI placed far away from all of the spheres, the pedestal and Compton region dominate, although the 364 keV photopeak is still discernible.

The scale factors for each of the five window-based scatter corrections are listed in Table 1. The scale factors were optimized for each view separately and for the combined data.

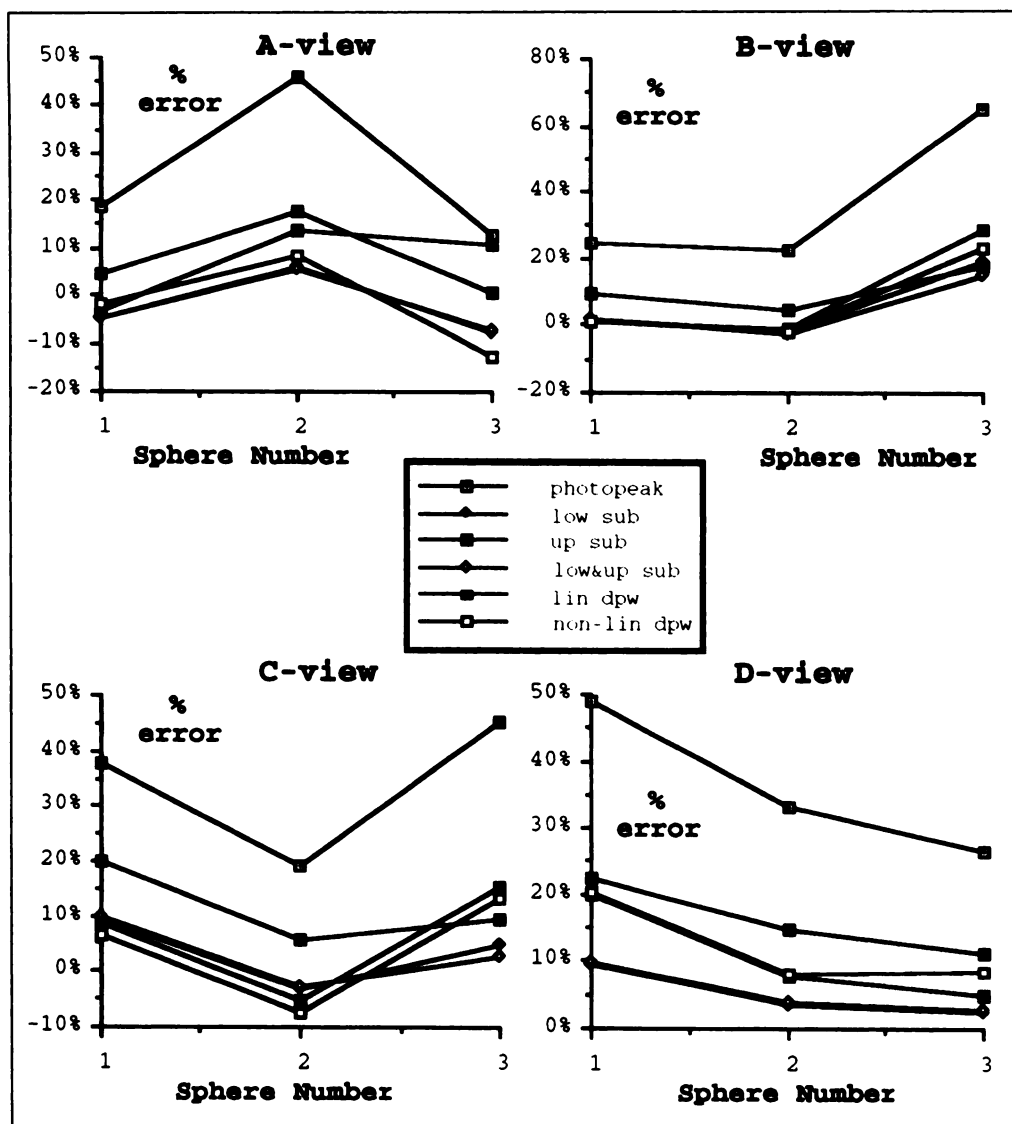


FIGURE 5. Window-subtraction results. These graphs display the resulting bias when the combined-optimization parameters (Table 1) are applied to ROIs for each of the three spheres in the elliptical phantom (Fig. 3).

Figure 5 shows the bias measured with the window-based scatter correction applied to ROIs in the three spheres (Fig. 3) using the parameters based on the combined data.

Spectrum-Fitting Scatter Correction

From the list-mode Rollo image data, images were generated containing a total of 1, 3 and 5 million counts in a 14% energy window centered at 364 keV. Unscattered counts were estimated with the split-pedestal model convolved with the EPSF, and the correlation coefficient error was calculated. The results are shown in Figure 6 where the error between the real image and the ideal image (1-CC) is plotted compared with the source depth. Two different approaches were used to derive the EPSF. One approach measured the EPSF using a flood source with the high energy collimator in place. The second fitted a Gaussian function to the energy spectrum of a point source in air without a collimator.

When the entire image is used in the correlation coefficient analysis, there is a large difference observed between the energy window and spectral fitting approaches (Fig. 6A). Much of this difference results from the reduction of scatter outside of the object. The differences are smaller with a ROI placed only around the Rollo phantom. This better reflects the clinical problem (Figs. 6B,C,D). The correction improves the images most in high-count, high-scatter situations, and least for low-count, low scatter situations. In the "no-scatter" case, the

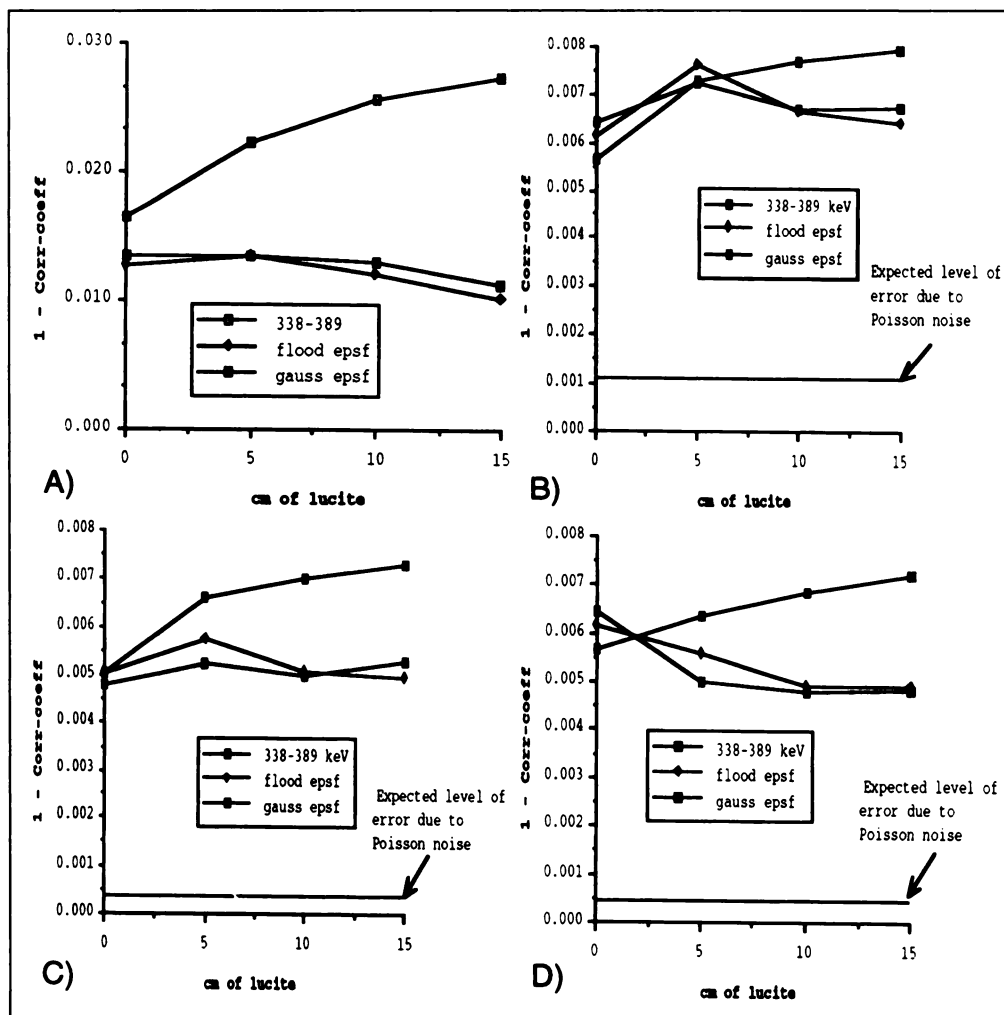
spectral-fitting bias is greater than or equal to the bias calculated for the 14% energy window; however, with scattering material the spectral fitting algorithm produces better results.

Visually, the area of the image outside the Rollo phantom was significantly improved (Figs. 7, 4C,D). Figure 4C shows a 5 M count image of the Rollo phantom with 15 cm of intervening lucite acquired using a 338–389 keV (14%) energy window. Figure 4D shows the result of the spectrum-fitting technique applied to the data in the 315–415 keV range (27% window). Figure 7 shows profiles through the regions of highest activity in the Rollo phantom (as indicated in Fig. 4). The profiles for the three datasets in each plot are normalized to the lowest activity region. The spectral fitting approach improves the profiles, but there is still some bias in the data as shown by the apparent underestimate of the activity in the hottest region.

DISCUSSION

The results from the hot spheres in the elliptical tank lead to two conclusions. First, septal penetration by 364 keV gamma rays is significant even at image locations far from the sources. Second, most of the 637 keV photons detected in the 364 keV photopeak window contain no useful spatial information. Comparing the multiwindow techniques (Table 1), we find that when the combined parameters were applied to a single view, quantitation errors ranged from -7% to +20%. Uncorrected

FIGURE 6. Examples of error measurements in images of the Rollo phantom as a function of the amount of scattering material between the phantom and the scintillation camera. (A) Error in 1.0 M count images (total image), calculated in the entire 128×128 image. (B): Error in 1.0 M count images (ROI), calculated in a square ROI enclosing the Rollo-phantom image. (C) Error in 3.0 M count images (ROI), calculated in a square ROI enclosing the Rollo-phantom image. (D) Error in 5.0 M count images (ROI), calculated in a square ROI enclosing the Rollo-phantom image.



photopeak windows were always high, typically by +20% to +50%. Thus, while the multiwindow approaches provided better quantitative data than simple energy windowing, the errors were still large and dependent on source position.

The spectrum-fitting approach improved image quality in all cases examined. The spectrum-fitting routine is capable of removing counts from areas containing no activity, and the cells of the Rollo phantom appear better differentiated. Spectrum-fitting, however, did not improve quantitation in low-count, low-scatter situations (e.g., 1,000,000 count equivalent image with 5 cm of Lucite).

In high-scatter situations (the usual case in clinical imaging), the spectrum-fitting routine improves quantitation and contrast. Although the split-pedestal model used in the spectrum-fitting routine may be too simple to accurately reflect the incident spectrum, increasing the number of model components (basis functions) increases the number of coefficients that need to be estimated. These estimates will be subject to greater variance. Given the limited information available in nuclear medicine image data, there is an inherent trade-off between model accuracy (bias) and noise (variance) in the final images.

The 315–415-keV energy range used for the spectrum-fitting method may not be optimal. It was chosen to be as wide as possible. Below 315 keV, the 284-keV emission contributes to the spectrum. The upper limit was determined by the upper-level discriminator on the GE 3000 XC/T; however, 415 keV is probably close to the window's upper limit because the Compton-edge of the 637 keV emissions occurs at 455 keV. At energies near the Compton-edge, the flat pedestal model would

be less accurate. It is possible to change the energy range of the GE Starcam systems (25) and we plan to pursue ^{131}I studies with a higher upper energy cutoff.

We are re-examining the behavior of our spectrum-fitting model with simulated data. We believe improvements in the model may be obtained by optimizing the observation window size, optimizing the bin-size in the observation window, improving the incident-spectrum (scatter) model, and using a spatially variant EPSF.

We also wish to determine the minimum number of energy bins that are needed. In a practical implementation of the spectrum-fitting approach, the use of list mode data would be cumbersome. Implementing a multiple energy window acquisition (an image for each window) and immediately processing the data after acquisition would be preferable. Thus, reducing the number of windows needed from the 25 used here would be desirable.

The software needed for performing the spectrum-fitting and subsequent scatter correction was written in Fortran 77. The code to bin the list mode $256 \times 256 \times 25$ (xyE) histograms required 4 min for the equivalent of a 5-million event image in a 14% energy window. The spectrum-fitting and subsequent formation of the final 256×256 image took 3 min. All computations were performed on a Data General AviiON 6200 series UNIX system running at 25 MHz.

CONCLUSION

We presented a comparison of multiwindow scatter approaches applied to ^{131}I filled spheres in an elliptical phantom.

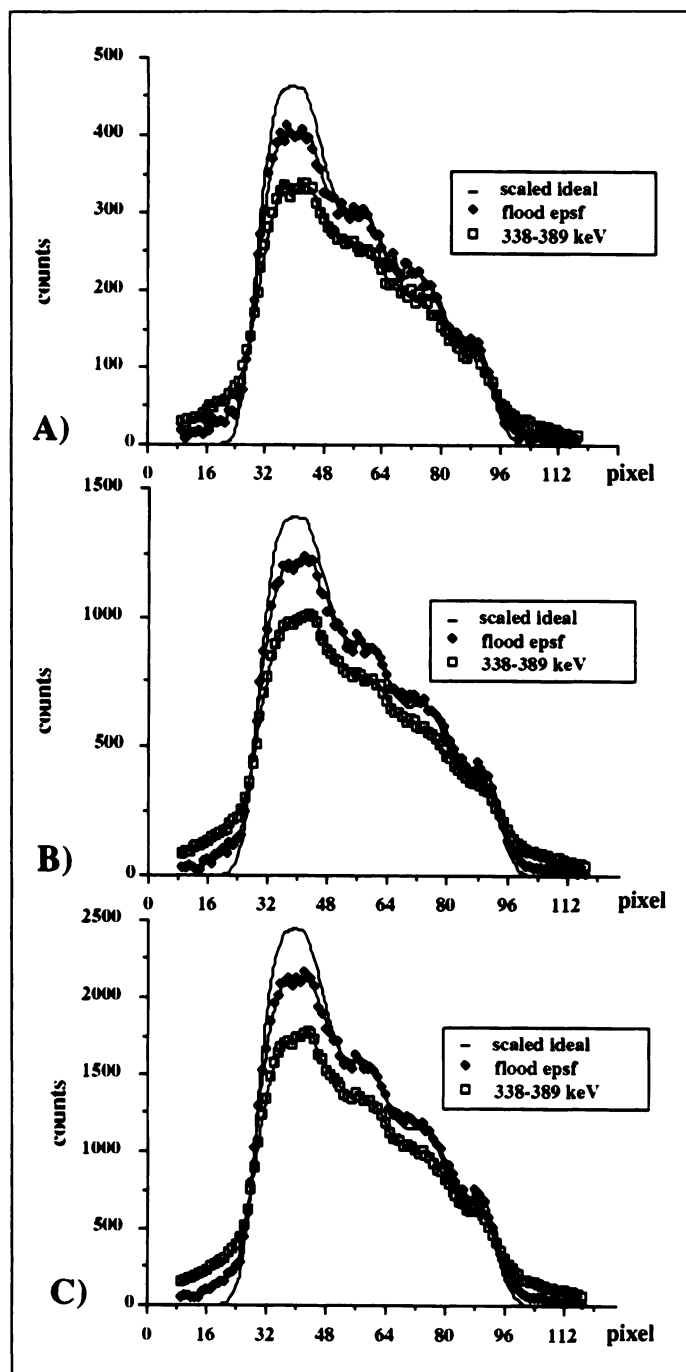


FIGURE 7. Profiles for the region of interest defined in Figure 4. The plots depict curves for a simple energy window (338–389 keV), scatter-corrected images using the spectrum-fitting model discussed in the text (flood EPSF), and the computer generated idealized phantom (Fig. 4B). (A) Results for 1 million counts in the image. (B) Results for 3 million counts. (C) Results for 5 million counts.

We also presented a scatter correction based on fitting the energy spectra at each pixel that was evaluated with a series of Rollo phantom images. While the spectrum-fitting approach improved quantitation in high-scatter situations, it still requires further development to reach our quantitative target in all parts of an image.

Optimizing the spectrum-fitting model and the fitting parameters may improve results in low-count, low-scatter situations. In particular, modifying an adaptive fitting approach recently proposed for ^{99m}Tc and ^{201}Tl (26) may improve performance for ^{131}I . Also, the spectrum-fitting approach used for the data in this article assumed that the photopeak position was spatially

invariant. From previous work, we know that the photopeak position in the camera used for this study varies by approximately ± 3 keV at different spatial locations. Recent work with ^{99m}Tc has shown that accounting for the spatial dependence of photopeak position improves performance and similar results may be obtained with ^{131}I .

We are continuing to improve the spectrum-fitting approach. We have modified two of our scintillation cameras to acquire list mode data for ^{131}I antibody studies. The results obtained thus far indicate that the spectrum-fitting approach results in less bias than other scatter correction schemes. In addition, the spectrum-fitting routine does not require phantom-based calibration factors. The EPSF and the spatial map of photopeak positions can be obtained during the normal energy calibration procedure used for most scintillation cameras. There are no further adjustments, phantom measurements, or other parameter changes regardless of the size of the patient or the distribution of the isotope. With further improvements in the spectrum-fitting approach outlined above, we hope to achieve our 5% bias goal and begin using this technique routinely in our ^{131}I patient scans.

ACKNOWLEDGMENTS

This work was supported by National Institutes of Health grants CA42593 and CA44991 and by General Electric Medical Systems.

REFERENCES

1. Eary JF, Press OW, Badger CC, et al. Imaging and treatment of B-cell lymphoma. *J Nucl Med* 1990;31:1257–1268.
2. Pollard KR, Bice AN, Durack LD, Eary JF, Lewellen TK. Camera-induced Compton scatter and collimator penetration in iodine-131 imaging [Abstract]. *J Nucl Med* 1992;33:889.
3. Pollard KR, Bice AN, Durack LD, Lewellen TK, Miyaoka RS, Kohlmyer SG. Using list-mode data to compare scatter corrections in ^{131}I imaging. *IEEE Medical Imaging* 1992;92CH32326:1111–1113.
4. Pollard KR, Haynor DR, Miyaoka RS, Kaplan MS, Lewellen TK, Harrison RL. Scatter correction in ^{131}I gamma camera images: subtraction-windows versus spectral-fitting [Abstract]. *J Nucl Med* 1993;34(suppl):60P.
5. Green AJ, Dewhurst SE, Begent RHJ, Bagshawe KD, Riggs SJ. Accurate quantification of ^{131}I distribution by gamma camera imaging. *Eur J Nucl Med* 1990;16:361–365.
6. Fleming JS, Alaamer AA, Perring S. A technique for the absolute quantification of ^{131}I radiopharmaceuticals using SPECT. *Nucl Med Commun* 1993;14:498–505.
7. Riggs SJ, Green AJ, Begent RH, Bagshawe KD. Quantitation in ^{131}I -radioimmuno-therapy using SPECT. *Int J Cancer Suppl* 1988;2:95–98.
8. Koral KF, Swaiman FM, Clinthorne NH, Rogers WL, Tsui BMW. Dual-window Compton-scatter correction in phantoms: errors and multiplier dependence on energy. *J Nucl Med* 1990;31:798–799.
9. Macey DJ, Bayouth J, Boyer A, Auster M. A new scatter correction method for quantitative ^{131}I spect imaging [Abstract]. *Med Phys* 1992;19:780.
10. Grant EJ, Macey DJ, Bayouth JE, Giap HB. A triple energy window scatter subtraction approach for quantitative angler camera imaging of iodine-131 [Abstract]. *J Nucl Med* 1994;35(suppl):142P.
11. Sorenson JA, Phelps ME. *Physics in nuclear medicine*, 2nd ed. Orlando: Grune and Stratton, Inc.; 1987:590.
12. Kibby PM. The design of multichannel collimators for radioisotope cameras. *Br J Radiology* 1969;42:91–101.
13. Ostertag HJ, Sroka-Perez G, Kubler WK. Results for a gamma-camera with a new 511-keV collimator. *Eur J Nucl Med* 1992;19:917–918.
14. Bice AN, Eary JF, Nelp WB. Quantification of iodine-131 distribution by gamma camera imaging. *Eur J Nucl Med* 1991;18:142–144.
15. Pollard KR. *Correction for Compton scatter in iodine-131 gamma camera images*. Thesis, University of Washington; 1994:1–166.
16. Jaszczak RJ, Greer KL, Floyd CE Jr, Harris CC, Coleman RE. Improved SPECT quantification using compensation for scattered photons. *J Nucl Med* 1984;25:893–900.
17. King MA, Hademenos GJ, Glick SJ. A dual-photopeak window method for scatter correction. *J Nucl Med* 1992;33:605–612.
18. Pentlow K. Effects of high-energy septal penetration and backscatter on quantitative imaging with ^{131}I [Abstract]. *Radiology* 1991;181:187.
19. Haynor DR, Harrison RL, Lewellen TK. SPECT scatter correction algorithms using position and energy information: preliminary simulation studies. *IEEE MIC Conf Proc* 1991;91CH31005:1803–1804.
20. Kaplan MS, Haynor DR, Lewellen TK, Pollard KR, Miyaoka RS, Harrison RL. Quantitative evaluation of an energy based scatter correction using planar rollo phantom images. *IEEE Trans Nucl Sci* 1994;41:1607–1611.
21. Haynor DR, Harrison RL, Lewellen TK. Scatter correction for gamma cameras using constrained deconvolution. *IEEE MIC Conf Proc* 1992;92CH32326:1132–1134.
22. Lewellen TK, Bice AN, Pollard KR, Zhu J-B. Evaluation of a clinical scintillation camera with pulse tail extrapolation electronics. *J Nucl Med* 1989;30:1554–1558.

23. Lewellen TK, Miyaoka RS, Kohlmyer SG, Pollard KR. An X-Y acquisition interface for General Electric Starcam Anger cameras. *IEEE MIC Conf Proc* 1991;91CH31005:1861-1865.
24. Rollo FD, Harris CC. Factors affecting image formation. In: Rolloe FD, ed. *Nuclear medicine physics, instrumentation and agents*. St. Louis: C.V. Mosby Co.; 1977:397.
25. Lewellen TK, Miyaoka RS, Kaplan MS, Kohlmyer SK, Costa WC, Jansen F. Preliminary investigation of coincidence imaging with a standard dual-headed spect system [Abstract]. *J Nucl Med* 1995;36(suppl):175P.
26. Haynor DR, Kaplan MS, Harrison RL, Lewellen TK, Harrison RL. Multiwindow scatter correction techniques in single photon imaging. *Med Phys* 1995;22:2015-2024.

Comparison of Continuous Step-and-Shoot versus Step-and-Shoot Acquisition SPECT

ZongJian Cao, Christophe Maunoury, Charles C. Chen and Lawrence E. Holder

Department of Diagnostic Radiology and the Cancer Center, University of Maryland Medical Center, Baltimore, Maryland

This study compared the quality of SPECT images obtained with step-and-shoot mode (SSM) and continuous step-and-shoot mode (CSSM). **Methods:** Computer simulations of SSM and CSSM were performed with a two-dimensional Shepp-Logan head phantom and a high-resolution parallel-hole collimator. The effects of noise and photon attenuation were examined. **Results:** Without noise and without attenuation, small structures in reconstructed images obtained using fast CSSM (less than 4 sec per view plus the moving time from one view to the next) were slightly blurred and rotated in the opposite direction of detector motion. With both noise and attenuation, these artifacts were not visible, and the image quality obtained from CSSM, especially from fast CSSM, was improved as compared to that resulting from the corresponding SSM due to the increasing number of counts. The improvement of image quality became less significant with increasing acquisition time and in the presence of attenuation. **Conclusion:** For fast SPECT, CSSM provided better image quality than the corresponding SSM, especially when attenuation effects were not present. For relatively long time SPECT without attenuation compensation that is typical for clinical studies, the image quality of CSSM was similar to that of SSM.

Key Words: SPECT; step-and-shoot; continuous acquisition

J Nucl Med 1996; 37:2037-2040

There are three modes of SPECT acquisition: step-and-shoot, continuous and continuous step-and-shoot. In the step-and-shoot mode (SSM), projection data are acquired only when the detector is stationary at sequential views. In the continuous mode (CM), data are acquired as the detector moves continuously. In the continuous step-and-shoot mode (CSSM), data are acquired both when the detector is stationary and when the detector moves from one view to the next. Bieszk and Hawman compared CM and SSM using simulation with an ideal pencil-beam collimator and using phantom studies with an ultra-high resolution collimator. They suggested that CSSM might have the sensitivity of CM, but with resolution approaching that of SSM (1). A clinical application of CSSM has also been reported (2). The purpose of our study was to compare the image quality and identify the strengths and weaknesses of CSSM versus SSM.

MATERIALS AND METHODS

The two-dimensional Shepp-Logan head phantom (3) used in this study was composed of six elliptical structures with different positions, orientations, sizes and activities (Table 1). To isolate the effects of detector motion in CSSM, statistical noise and photon attenuation, simulations were performed without noise and without

attenuation, with noise and without attenuation, and with noise and with attenuation. A high-resolution collimator was used in the simulations. The data were acquired with 64 views over 360° and with an array of 64 pixels at each view. The time needed to move the detector from one view to the next was set to 4 sec which is typical for most commercial SPECT systems. For SSM, the acquisition times were chosen to be 25, 15, 4 and 1 sec per view. For CSSM, the acquisition time was equal to the SSM time-per-view plus the moving time of the detector, so the corresponding acquisition times were 25 + 4, 15 + 4, 4 + 4 and 1 + 4 sec, respectively.

To simulate continuous acquisition between two adjacent views, the angle between the two views was divided into a number of intervals. The detector stopped and acquired data at the center of each interval. The discrete acquisition mode becomes more continuous with increasing number of intervals. In this study, 8, 16 and 24 intervals were tried for 1 + 4-sec CSSM, and little difference was found among the images visually and quantitatively. Therefore, eight intervals were used to decrease processing time. The projection data were acquired at the midpoint of each interval (the dots in Fig. 1) for 0.5 sec. The angular positions of these midpoints were

$$\varphi_i + \frac{5.625^\circ}{16}, \varphi_i + \frac{5.625^\circ \cdot 3}{16}, \dots, \text{and } \varphi_i + \frac{5.625^\circ \cdot 15}{16},$$

where φ_i and φ_{i+1} were the angular positions of two adjacent views and the angle between φ_i and φ_{i+1} was 5.625° (=360°/64 views).

TABLE 1
Geometric Parameters Used for the Ellipses in the Two-Dimensional Shepp-Logan-Head Phantom

Ellipse	Semiaxes a and b (cm)	Position of center x and y (cm)	Vertical angle* (°)	Activity weight† (1/cm)
1	a = 11.56, b = 14.75	x = 0, y = 0	0	2
2	a = 11.00, b = 14.12	x = 0, y = 0.25	0	-1
3	a = 2.69, b = 6.12	x = -3.56, y = 0	-18	-1
4	a = 2.12, b = 4.75	x = 3.56, y = 0	18	-1
5	a = 3.75, b = 4.06	x = 0, y = 7.5	0	1
6	a = 0.62, b = 0.62	x = 0, y = -8.75	0	2

*The vertical angle is defined as the angle between the vertical direction and the long axis of an ellipse.

†The activity weight of Ellipse 2 is relative to that of Ellipse 1 and the activity weights of Ellipses 3, 4, 5 and 6 are relative to that of Ellipse 2. For example, the activity of Ellipse 2 is 1 (=2 - 1) and the activity of Ellipse 3 is 0 (=1 - 1). The expression is mathematically convenient for computing the sum of activity along an intersecting ray.

Received July 24, 1995; revision accepted Oct. 18, 1995.

For correspondence or reprints contact: ZongJian Cao, PhD, Department of Radiology, University of Maryland Medical Center, 22 South Greene St., Baltimore, MD 21201.